SPECIAL TOPIC — A 40th Anniversary Celebration: Physics Research and Innovation at Ningbo University

Stretchable bionic motion sensory neuron established with stretchable resistive sensors

Wan-Lin Zhang(张万林), Si-Yuan Zhou(周思远), Bei-Chen Gong(龚北辰), Bo-Bo Li(李波博), Lin-Feng Wu(吴林枫), Ya-Rong Yuan(袁亚蓉), Chen-Rui Zhai(翟晨芮), Yu-Fan Hu(胡宇凡), and Li-Qiang Zhu(竺立强)†

School of Physical Science and Technology, Ningbo University, Ningbo 315211, *China*

(Received 10 March 2026; revised manuscript received 20 April 2026; accepted manuscript online 6 May 2026)

Due to the well-known von Neumann bottleneck, there is an urgent need for a sensing-computing-integrated architecture with low power consumption and low latency to handle data in real time. Inspired by brain information processing, a stretchable bionic motion sensory neuron is proposed by integrating solution-processed chitosan-gated oxide neuromorphic transistors and a stretchable resistive sensor (SRS). The SRS is fabricated using Ecoflex silicone as a substrate, doped with carbon black and multi-walled carbon nanotubes. It demonstrates high sensitivity with a gauge factor of up to 32, offering a wide detection range with mechanical tensile strain of up to 200%. Notably, it has a response time of only 173 ms and outstanding durability over 3000 stretch-release cycles. The bionic motion sensory neuron can accurately sense external strain and exhibit typical synaptic responses with strain applied to the SRS. Since strain can carry information, it demonstrates signal encryption and decoding capabilities. Moreover, it can monitor joint bending activities in real time. Thus, the sensory neuron holds potential for wearable electronics, neural prosthetics, and intelligent human-machine interfaces.

Keywords: stretchable bionic motion sensory neuron, neuromorphic transistors, stretchable resistive sensor, motion monitoring

PACS: 85.30.Tv

DOI: 10.1088/1674-1056/ae6902 **CSTR:** 32038.14.CPB.ae6902

1. Introduction

The rapid advancements in artificial intelligence, the Internet of Things, and wearable technology have imposed stringent demands on information processing platforms.[1,2] However, conventional von Neumann architecture, which has dominated the computing landscape for decades, necessitates frequent data transfers due to the physical separation of computing units and storage units.[3] This not only results in substantial energy consumption but also significantly increases data processing delays. The bottleneck is particularly pronounced in edge computing scenarios that require real-time perception, learning, and decision-making.[4,5] Brain-inspired computing can emulate the architecture of biological nervous systems, offering advantages including integrated storage and computing, low power consumption, and parallel processing.[6,7] It is considered a pivotal approach to overcoming the von Neumann bottleneck. Since neurons and synapses are the basic functional units of brain computing, hardware-based neuromorphic devices have been proposed, including two-terminal memristor- based ones[8–10] and three-terminal transistor-based ones.[11–14] Moreover, optoelectronic devices[15,16] and spintronic devices[17,18] have also been proposed for neuromorphic applications. Basic synaptic responses, advanced neuromorphic functions, and neuromorphic computing have been demonstrated, showing significant potential for advanced energy-efficient computing.

Meanwhile, our nervous system is a complicated and collaborative perceptual processing system. Our specialized receptors in sensory organs can detect diverse environmental stimuli. They transduce these signals into interpretable sensory information. Such information is then sent to the brain for cognitive processing. Thus, sensory cognitive activities are realized.[19] Inspired by the brain's cognitive perceptual system, bionic perceptual platforms have been proposed by integrating neuromorphic devices with sensors, including mechanical sensors, chemical sensors, and optosensors, to establish tactile, visual, auditory, olfactory, and gustatory perceptual systems.[8,13,20–22] Moreover, multi-modal neuromorphic perceptual platforms have been proposed, including bionic auditory-tactile bimodal perceptual platforms,[23] bionic visual-tactile bimodal perceptual platforms,[24,25] bionic visual-thermal bimodal perceptual platforms,[26,27] etc. In these bionic perceptual platforms, the sensors can transduce external signals into electrical signals. The artificial synapses can process these signals in a manner similar to that of biological neural systems. Thus, high-speed, efficient, and low-energy parallel processing can be achieved across multiple spatiotemporal scales, which is meaningful for cognitive interactive platforms.

Strain sensors play a significant role in wearable

†Corresponding author. E-mail: zhuliqiang@nbu.edu.cn

© 2026 Chinese Physical Society and IOP Publishing Ltd. All rights, including for text and data mining, AI training, and similar technologies, are reserved.

CPB Online In-Press

technology,[28] human-computer interaction,[29] and physiological signal monitoring.[30] It should be noted here that most strain sensors are made of metal and semiconductor materials, possessing inherent limitations in tensile strength and durability.[31–33] Thus, it is difficult to adapt to the development of flexible intelligent electronic devices under stretching, twisting, and folding. In contrast, stretchable strain sensors made of advanced flexible materials have advantages, including a wide tensile strain range, high sensitivity, fast response speed, high stability, and high durability. They have received attention in fields including medical health,[34] sports monitoring,[35] intelligent robots,[36] electronic bionic skin,[37] and human-computer interaction.[38] However, existing stretchable sensor-based neuromorphic systems still face some limitations. Most stretchable strain sensors involve a trade-off between sensitivity and stretchability. And most reported systems focus on basic sensing or single-function imitation, seldom demonstrating complex biomimetic behaviors. Thus, building "sensing-computing" systems capable of simultaneously achieving signal sensing, amplification, and processing represents a crucial research branch in neuromorphic electronics. Additionally, electrolyte-gated transistors possess unique interfacial ionic coupling effects, demonstrating great potential in neuromorphic electronics, including low operation voltage, abilities to mimic short-term/long-term synaptic plasticity, and advanced learning activities.[11] Thus, electrical outputs from stretchable strain sensors could act as inputs for the electrolyte-gated transistors, demonstrating potential in bionic sensory platforms.

Thus, the present work proposes a stretchable bionic motion sensory neuron with the following distinct achievements. (i) In terms of material synergy, the fabricated stretchable resistive sensor (SRS) simultaneously achieves a high gauge factor of ~ 32 and a wide strain range of up to 200% by combining carbon black (CB) and multiwalled carbon nanotubes (MWCNTs) in an Ecoflex matrix. (ii) In terms of passive integration scheme, the SRS and the chitosan gated indium tin oxide (ITO) neuromorphic transistor are coupled via a simple voltage divider circuit without any active signal conditioning, enabling direct conversion of mechanical strain into synaptic responses. (iii) In terms of advanced bionic functions, the system demonstrates intelligent motion classification using a ResNet 1D model with high accuracy. A series of sophisticated, brain inspired behaviors have been demonstrated on a single stretchable neuromorphic platform, including Morse-code encoding/decoding, electronic emulation of nociceptive behavior, and "learning-forgetting-relearning" functionalities. Table S1 shows a comparison of reported stretchable sensors and bionic perceptual platforms. The present sensor shows comparable properties and multiple bionic functions. Therefore, the bionic system demonstrates potential in fields of wearable electronic devices, neural prostheses, and intelligent human-machine interfaces.

2. Experimental details

2.1. Fabrication of stretchable resistive sensory platform

An ITO ionotronic neuromorphic transistor was obtained using a low-cost process. Figure 1(a) schematically illustrates the fabrication process. First, 2 wt% chitosan (Degree of deacetylation: $\sim$ 86%, Tokyo Chemical Industry Co.) and 2 wt% acetic acid (Ourchem) were dissolved in 96 wt% deionized water to obtain a chitosan solution. After standing for 24 hours, the solution was drop-cast onto an ITO glass substrate and dried in an oven at 45 °C for 7 hours to form a solid-state chitosan-based electrolyte film. Next, patterned ITO electrodes were obtained by sputtering an ITO target (In_2O_3:SnO_2 = 90:10 wt%). Due to the reflection of sputtered ITO nanoparticles at the mask edge, a thin ITO channel layer

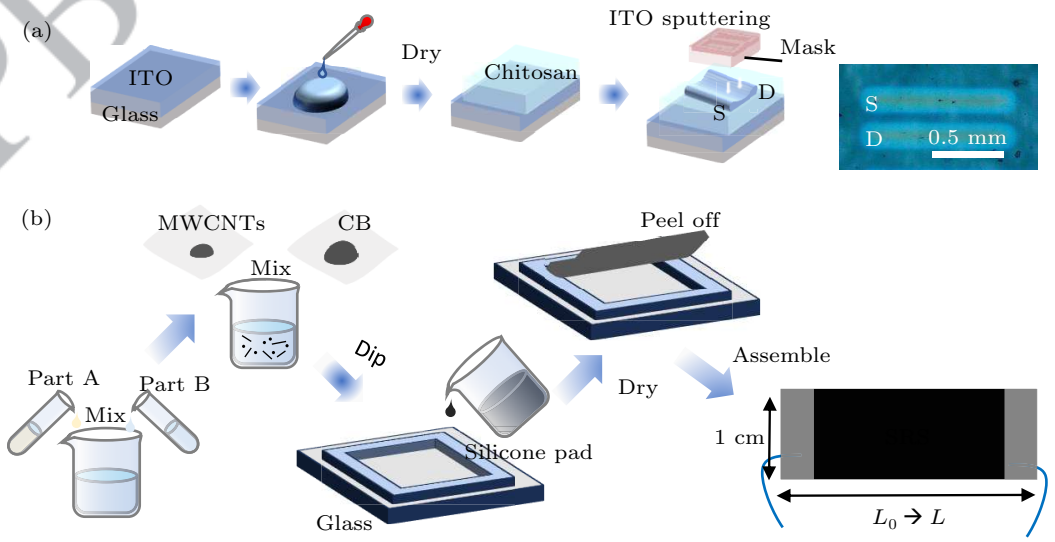


Fig. 1. (a) Flowchart of the fabrication of ITO ionotronic neuromorphic transistors. Right inset: CCD image of an ITO neuromorphic transistor. (b) Flowchart of the fabrication of Ecoflex/CB/MWCNTs-based SRS.

CPB Online In-Press

can be formed between two patterned ITO electrodes, i.e., source (S) and drain (D) electrodes. The sputtering pressure, DC sputtering power, and argon flow rate were set at 0.8 Pa, 80 W, and 40 sccm, respectively. The charge-coupled device (CCD) image of the ITO ionotronic neuromorphic transistor is shown in the right inset of Fig. 1(a). The channel width and length are $\sim$ 1000 μm and $\sim$ 80 μm, respectively.

Ecoflex/CB/MWCNTs-based stretchable resistive sensor (SRS) was obtained using a solution-based process. Figure 1(b) schematically illustrates the fabrication process. First, Ecoflex 00-30 silicone rubber solution (Smooth-On) Part A (Platinum Catalyst) and Part B (Vinyl-terminated PDMS/Hydrosilylation Agent) were mixed at a mass ratio of 1:1 and stirred for 5 minutes to ensure uniform mixing. Then, nanogranular CB was added to the mixture at a mass ratio of 1:20, followed by the addition of MWCNTs at a mass ratio of 1:100. The mixture was stirred for 10 minutes to form a uniform solution. Next, the prepared solution was degassed using a vacuum pump. Then, it was blade-coated onto a silicone mold with a size of 5 cm $\times$ 5 cm. After being left at room temperature for 24 hours, the cured membrane was peeled off from the silicone mold. It was cut into strips with a size of 5 cm $\times$ 1 cm. Copper tape was then attached to both ends and connected to wires to create an SRS. At last, a sensory platform was obtained by integrating the SRS and the ITO ionotronic neuromorphic transistor together.

2.2. Characterization and measurements

The thickness of the chitosan film was characterized using scanning electron microscopy (SEM: SU-70). The frequency-dependent capacitance of the chitosan-based electrolyte film was characterized using an impedance analyzer (IM3533). A linear motor (LPS1.2) was used to apply tensile force to the SRS. Bionic synaptic responses and advanced neuromorphic functions of the stretchable bionic motion sensory neuron were characterized using a semiconductor parameter analyzer (Keithley 4200A SCS). The partial voltage of the SRS was measured using an oscilloscope. All the electrical measurements were carried out under air with a relative humidity of $\sim$ 50%.

2.3. Results and discussion

In recent years, stretchable mechanical sensors have been widely adopted in wearable technologies. Excellent mechanical properties and conductivity are important for sensitive strain sensors. Figure 2(a) shows a schematic diagram of the sensing mechanism for the present SRS. The conductive components within the flexible Ecoflex matrix are formed by the combination of CB particles and MWCNTs, creating a highly conductive network. This network enables conduction between CB and CB, MWCNTs and MWCNTs, as well as CB and MWCNTs. From a microscopic perspective, the changes in the conductivity of the conductive network are mainly related to the separation of CB nanoparticles and MWCNTs.[39–41] When the sensor is not stretched, adjacent CB particles or adjacent MWCNTs are in close contact with each other, resulting in high conductivity. As the tensile strain gradually increases, adjacent CB particles begin to separate, while adjacent MWCNTs slide and separate from each other, ultimately leading to a break in the conductive network. The center distance (d) between two adjacent CB particles can be classified into three types,[42–44] i.e., (i) adjacent CB particles in complete contact, (ii) adjacent CB particles not in contact but within a certain cutoff distance (C), and (iii) adjacent CB particles completely disconnected. When d is comparable to the diameter (D) of a CB particle of $\sim$ 50 nm, the CB particles exhibit complete contact. When d is larger than D but smaller than the C value, tunneling current still exists between the conductive particles due to the electron tunneling effect. Finally, when d is greater than C, CB particles are completely disconnected, resulting in an extremely low current. In addition, when the flexible Ecoflex matrix is stretched, the columnar MWCNTs in the conductive network slide against each other, gradually reducing the overlapping area until they are completely separated. Therefore, the conductive layer of the sensor exhibits the highest conductivity when there is no stretching. As the strain increases, the distance between adjacent CB particles gradually increases. In addition, the overlapping area between adjacent columnar MWCNTs decreases with strain. All these effects result in increased resistance. Once the strain reaches a certain threshold, the CB particles and columnar MWCNTs are completely separated, resulting in the loss of sensing ability. After the stretching is released, the Ecoflex matrix reconstructs a well-connected conductive network, transforming from a completely separated state to a fully connected state and restoring good conductivity.

Here, mechanical tensile strain (ε) is defined as

$$\varepsilon = (L - L_0)/L_0, \tag{1}$$

where L and L_0 represent the length of the sensor with and without strain, respectively. Figure 2(b) shows the current–voltage (I–V) curves under different ε values. It is obvious that ohmic contact is observed, demonstrating decreased conductivity at increased ε values. The resistance (R) is $\sim$ 13 kΩ at $\varepsilon = 0$. While it increases to $\sim$ 536 kΩ at $\varepsilon = 200\%$. The change (η) in resistance is defined as

$$\eta = (R - R_0)/R_0 \times 100\%, \tag{2}$$

where R and R_0 represent the resistance with and without strain, respectively. Figure 2(c) shows the relationship between the η values and the ε values. It can be seen that the η value increases from $\sim$ 0% to $\sim$ 3982% with the increased

CPB Online In-Press

ε value from 0 to 200%. The sensitivity, i.e., gauge factor (GF), is defined below:[45]

$$\mathrm{GF} = \Delta\eta/\Delta\varepsilon. \tag{3}$$

Thus, two sensing ranges are exhibited. For the strain below 100%, the GF value is ~ 6.4. While for the strain ranging between 100% and 200%, the GF value is ~ 32.2. At low strain below 100%, the conductive mechanism is associated with the slight displacement of the CB particles. At this stage, the MWCNTs network is quite stable. Thus, the changes in resistance remain small. While at higher strain above 100%, the conductive mechanism is associated with the slipping of the columnar MWCNTs. At this stage, the columnar MWCNTs begin to separate, causing severe damage to the conductive network. Thus, the changes in resistance become significant. This enables the sensor to have a relatively high sensitivity. Figure 2(d) shows dynamic η values at different ε values. The η value increases with increased ε and then returns to the initial value upon releasing. The behavior exhibits clear repeatability across different cycles, indicating excellent sensing performance.

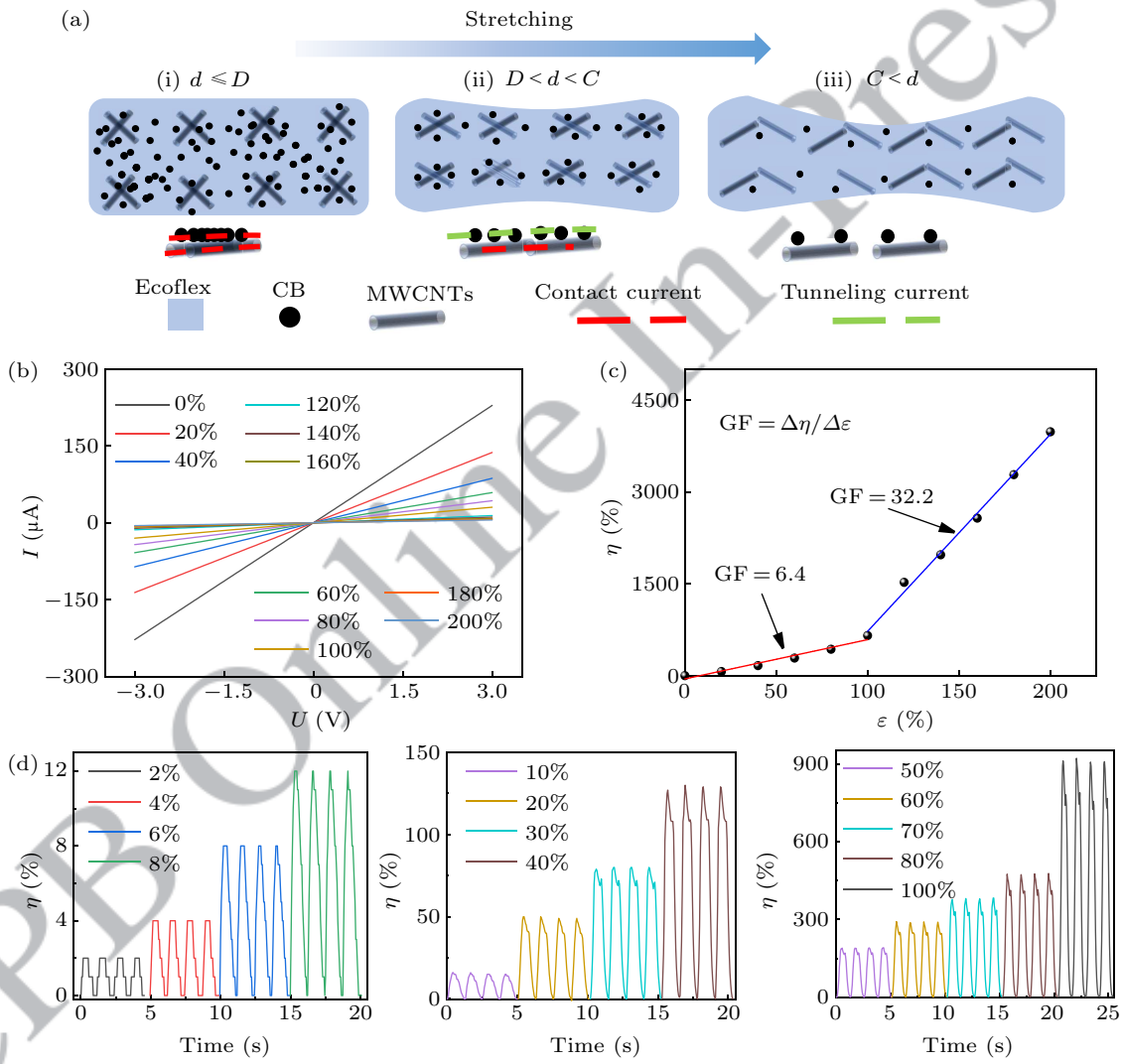


Fig. 2. (a) Schematic diagram of the sensing mechanism of the SRS. (b) Current–voltage (I–V) curves under different tensile strains (ε). (c) η values as a function of ε. (d) Dynamic η values at different ε values ranging between 2% and 100%.

In addition to high sensitivity and a wide strain sensing range, other properties should also be considered, including environmental adaptability, durability, and response time. Figure 3(a) shows a photograph of the SRS at the original state and under stretching. Figure 3(b) shows I–V characteristics of the SRS under strain with ε values of 20% and 40% after washing and sunlight exposure. Under the same ε value, the I–V curves approach each other very well, indicating stable performance. This also suggests the suitability for outdoor wearable applications. Figure 3(c) shows the dynamic η response at an ε value of 2%. At the rising stage, the response time is as short as ~ 173 ms. Due to the viscoelastic hysteresis of the membrane, i.e., the delayed reconstruction of the conductive network, the response time is prolonged to ~ 1.4 s upon the unloading of the stretching. To test the durability of the SRS, more than 3000 stretching and releasing cycles were carried out under strain with an ε value of 15%, as shown in Fig. 3(d). The peak η values remain at $\sim 30\%$ with a negligi-

CPB Online In-Press

ble drift of less than 3%. The baseline resistance recovered to its initial value after each cycle, indicating excellent repeatability and minimal hysteresis. Under continuous stretching, CB and MWCNTs underwent minor slip, while the Ecoflex matrix exhibited slow creep. The conductive network continued to undergo slight optimization, resulting in a gradual and stable decline in resistance without significant abrupt changes. At higher cycle numbers, the conductive filler achieved dynamic mechanical equilibrium within the Ecoflex soft matrix. The filler's dispersion, interlayer stacking, and densification reached saturation states, while residual stresses in the Ecoflex matrix were fully released. Creep and stress relaxation processes ceased, and the conductive network structure stabilized. Each tensile-recovery cycle demonstrated reversible deformation. The resistance baseline maintained stability, and drift phenomena were virtually eliminated. Figure 3(e) shows continuous cycling tests of the SRS under strain with an ε value of 50% at different stretching-releasing frequencies. When the frequency increases from 0.2 Hz to 1.0 Hz, the peak η values are always $\sim$ 170%. Additionally, the η values return to the same level when the strain is released, independent of the frequency. This indicates the good stability of the present SRS.

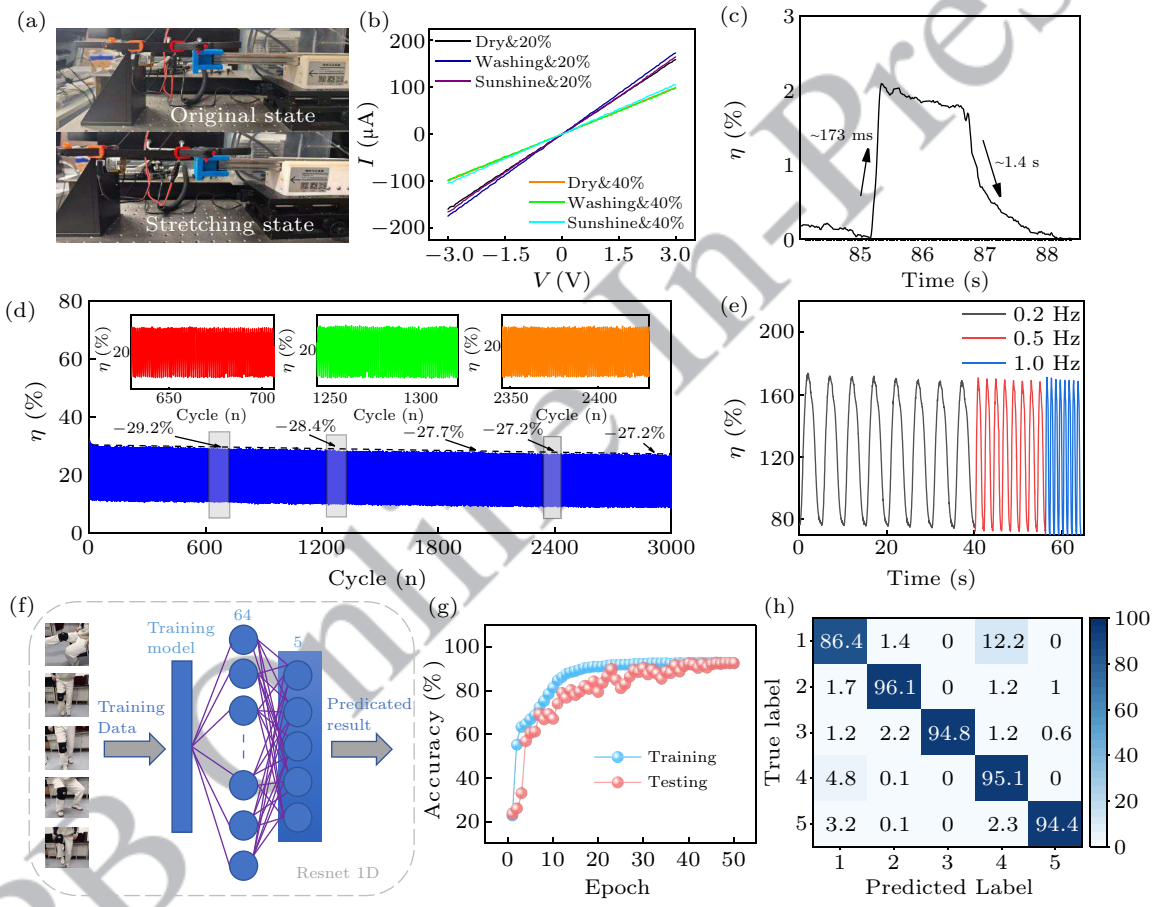


Fig. 3. (a) A photograph of the SRS in the original state and under stretching. (b) *I*–*V* curves of the SRS under strain with ε values of 20% and 40% after washing and sunlight exposure for 4 h. (c) Dynamic η response at an ε value of 2%. (d) Dynamic η response at an ε value of 15% under 3000 stretching-releasing cycles. (e) Dynamic η response at an ε value of 50% at different stretching-releasing frequencies. (f) Simplified schematic diagram of the 1D Residual Net for the recognition of movement instructions. (g) Average accuracy for the 5 movement instructions. (h) Confusion matrix of the training results for the 5 movement instructions.

Interestingly, the SRS is attached to the knees to detect different types of movements. With varied stretching lengths and frequencies at different movement states, resistance response characteristics can be recorded. A machine learning model can thus accurately distinguish these movement states.[46,47] Figure 3(f) shows the schematic diagram of the 1D Residual Net for the recognition of movement instructions. First, current responses under 5 different knee flexion movements from two volunteers were recorded, i.e., seated leg extension, small-step run, small-step walk, squat, and high-knee run. Figures S1 and S2 in Supporting Information show the corresponding dynamic η responses. After that, the data were sliced and normalized with a slice window length of 5000 and a step size of 75, obtaining 4315 slice samples. After preprocessing, these data were randomly divided into training and testing sets at a ratio of 8:2. Here, five-fold cross-validation was performed to reduce experimental randomness. During the training and evaluation stages, a cross-entropy loss function and a stochastic gradient descent optimizer were used. After each training epoch, the classification accuracy was evaluated on an independent test set. To comprehensively analyze the performance of the model, accuracy curves were recorded

CPB In-Press

to monitor the training process, as shown in Fig. 3(g). After 30 training epochs, the training accuracy exceeded 90%. At the same time, the testing accuracy was similar to the training accuracy, indicating good classification performance. Additionally, a confusion matrix was generated to intuitively show its classification performance for each instruction category. Figure 3(h) shows the confusion matrix for the 5 movement instructions. The overall recognition accuracy was $\sim$ 92%, indicating that the SRS has strong prospects in the field of intelligent sensing.

Figure 4(a) shows the frequency-dependent specific capacitance of the chitosan-based electrolyte film. A high specific capacitance of ~ 4.3 μF/cm^2 is obtained at 1 Hz. Such a high capacitance is related to the electric double layer (EDL) formed at the chitosan/ITO interface. Figure 4(b) shows the output characteristics of the ITO ionotronic neuromorphic transistor with V_{gs} increased from −0.6 V to 1.2 V in steps of 0.2 V. At low V_{ds}, good linearity is observed, indicating good ohmic contact. Good current saturation behavior is also observed at higher V_{ds}. All these results indicate good transistor performance. Figure 4(c) shows five repeated transfer curves measured at a fixed V_{ds} of 1.5 V. There is an anticlockwise hysteresis window of $\sim$ 0.2 V. The behavior is attributed to proton migration within the chitosan-based electrolyte. The on/off ratio, subthreshold swing, threshold voltage, and mobility are $\sim 4.9\times10^6$, $\sim$ 80 mV/dec, ~ -0.39 V, and ~ 5.8 cm$^2\cdot$V$^{-1}\cdot$s^{-1}, respectively. The proton-related interfacial EDL coupling endows the chitosan-gated ITO ionotronic neuromorphic transistors with the ability to mimic synaptic plasticity, including short-term synaptic plasticity (STP) and long-term synaptic plasticity (LTP).[48,49] Figure 4(d) demonstrates a typical excitatory postsynaptic current (EPSC) response triggered by a single gate spike (1 V, 10 ms). Figure 4(e) presents an EPSC response triggered by paired gate spikes (1 V, 10 ms) with an interval time (ΔT) of 10 ms. The second absolute EPSC value (A2) is higher than the first one (A1), i.e., ~ 3.35 μA vs. ~ 1.86 μA, well mimicking the paired-pulse facilitation (PPF) effects in biological nerve systems. Thus, the PPF index, defined as A2/A1 × 100%, is $\sim$ 180%. Figure 4(f) illustrates the PPF index as a function of ΔT. The behavior is highly similar to that of biological synapses[50] and the reported neuromorphic devices.[51,52] Figures S3(a) and S3(b) also show transfer curves and EPSC responses on five different transistors. The slight shifts are due to slight differences in the channel thickness. Figure S3(c) shows 40 EPSC responses obtained on a single device, exhibiting excellent stability. Figures S4(a) and S4(b) show spike number-dependent EPSC responses and spike amplitude-dependent EPSC responses, respectively. These results well mimic the transition from short-term memory (STM) to long-term memory (LTM). Figure S4(c) shows a typical EPSC response triggered by a presynaptic spike (10 mV, 10 ms) at V_{ds} of 0.01 V. The peak EPSC value is $\sim$ 2.5 nA. The energy consumption (P) is $\sim$ 250 fJ.

Left panel of Fig. 5(a) schematically shows the human motion-sensing neuron. First, primary sensory neurons located at the sensory organs specifically detect mechanical stimuli and convert them into electrical signals. These signals are then transmitted to the spinal cord or brainstem for real-time integration and processing. Finally, precise motor commands are issued by the spinal cord, transmitted through the neuromuscular junction to skeletal muscle fibers, and drive muscle contraction. This completes a closed-loop system from sensory input to motor output.[53] Here, a stretchable bionic motion sensory neuron is established by connecting the SRS with the ITO ionotronic neuromorphic transistor, as schematically shown in the right panel of Fig. 5(a).

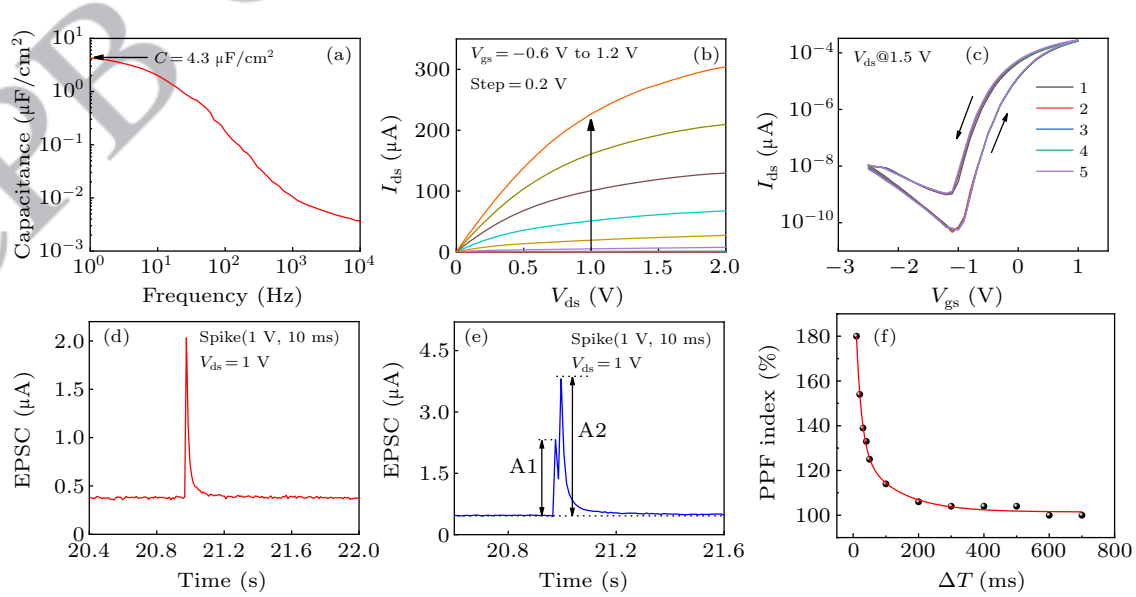


Fig. 4. (a) Frequency-dependent specific capacitance of the chitosan-based electrolyte film. (b) Output curves and (c) transfer curves of the ITO ionotronic neuromorphic transistor. (d) Typical EPSC response triggered by a single gate spike (1 V, 10 ms). (e) EPSC response triggered by paired gate spikes (1 V, 10 ms) with an interval time (ΔT) of 10 ms. (f) PPF index as a function of ΔT.

CPB Online In Press

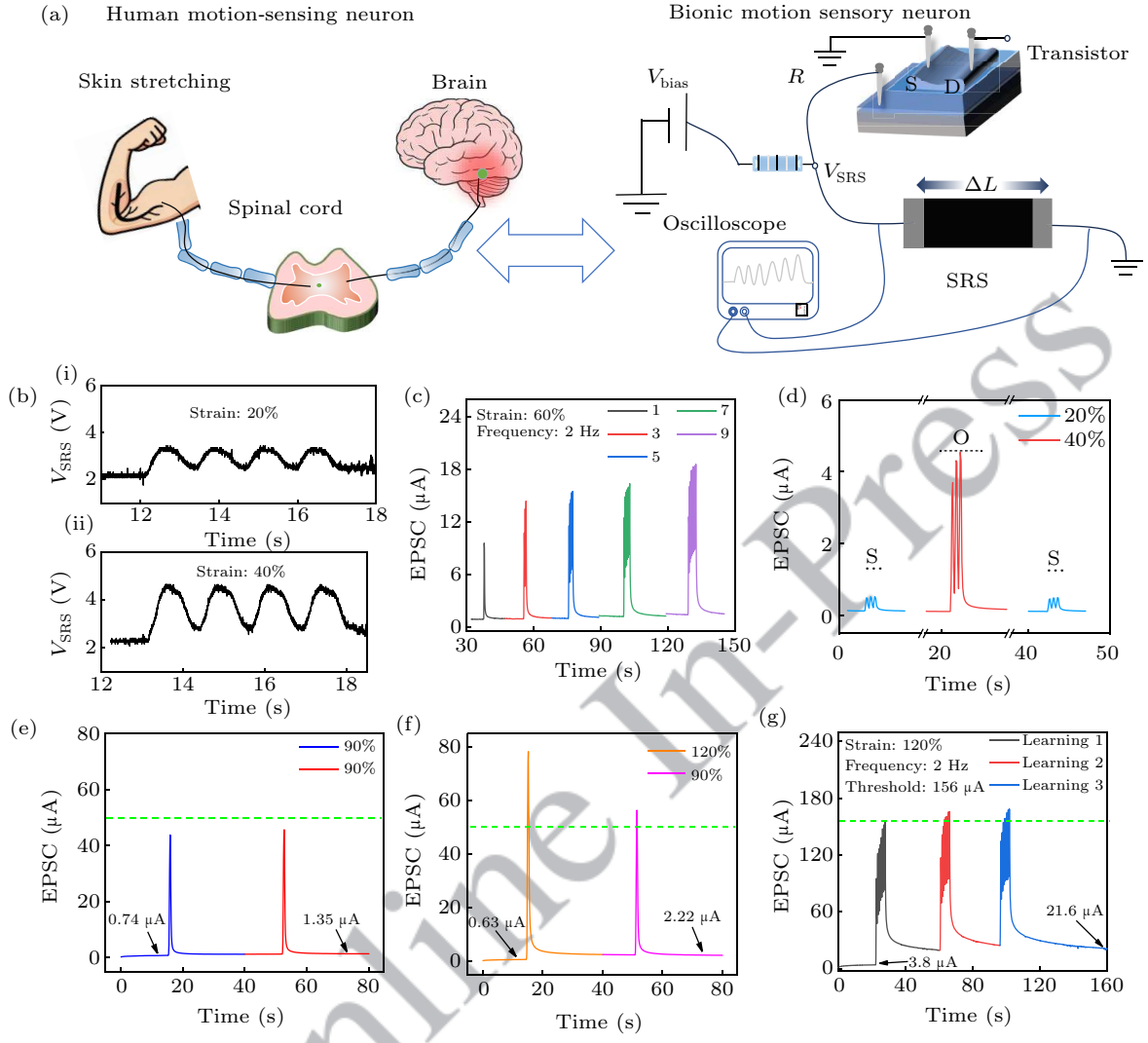


Fig. 5. (a) Schematic diagram of the human motion-sensing neuron and the stretchable bionic motion sensory neuron. (b) Dynamic divided voltage (V_{SRS}) on the SRS under repeated stretching. (c) Strain number-dependent EPSC responses under ε of 60%. (d) EPSC responses under ε of 20% and 40%, decoding Morse code "SOS". (e) EPSC responses triggered by applying a single "non-injury" stretching strain (90%) after experiencing "non-injury" strain (90%). (f) EPSC responses triggered by applying a single "non-injury" stretching strain (90%) after experiencing "injury" strain (120%). (g) Electronic emulation of "learningforgettingrelearning" dynamics based on proton cumulative modulation.

Under V_{bias} of 8 V, the divided voltage (V_{SRS}) across the SRS is loaded on the gate of the transistor, controlling the channel conductivity. When an external stretching force is applied to the SRS, changes in the resistance of the SRS trigger a voltage pulse on the gate, achieving dynamic field-effect modulation. Figure 5(b) shows the dynamic V_{SRS} under stretching. It is stable at ε values of 20% and 40%, with V_{SRS} values of $\sim$ 3.4 V and $\sim$ 4.5 V, respectively. Figure S5 shows the dynamic V_{SRS} under stretching with ε ranging from 60% to 120%, showing increased V_{SRS} values with increasing ε. The increased V_{SRS} value under strain is consistent with the increased resistance of the SRS under stretching. Rationally speaking, the V_{SRS} can also be modulated by V_{bias}. The corresponding V_{SRS} can trigger the migration of protons and the EPSC responses in the channel due to the EDL effects. This indicates that the SRS is feasible for regulating the neuromorphic device. Under dynamic stretching, a postsynaptic current (PSC) response can be generated. When the stretching force is released, the V_{SRS} returns to the resting level. Thus, the PSC also returns to the resting level. This is the main mechanism for the integrated system. Figure S6 shows the ε -dependent EPSC responses at V_{bias} of 6 V. As ε increases from 10% to 100%, the peak EPSC value increases from $\sim$ 0.175 μA to $\sim$ 69.05 μA. Figure 5(c) shows strain number-dependent EPSC responses at the same ε value of 60%. The frequency of the dynamic strain is 2 Hz. As the number of stretching cycles increases from 1 to 9, the peak EPSC value rises from $\sim$ 9.6 μA to $\sim$ 18.6 μA. This is due to the proton accumulation at the chitosan/channel interface. Morse code is an internationally recognized communication language that uses dots and dashes to represent various characters. Interestingly, the present artificial neuron possesses potential for encoding and decoding information. Here, signals, i.e., dots and dashes, are represented by tensile strains with ε values of 20% and 40%, respectively. By stretching the sensor regularly, signals can be recognized by the EPSC value. EPSC values below 3 μA and above 3 μA are associated with dots

CPB Online In-Press

and dashes, respectively. Figure 5(d) shows EPSC responses under strains. These EPSC responses can be decoded as the word "SOS".

The present bionic motion sensory neuron can also emulate certain features of nociceptive behavior in an electronic analogue scheme.[54,55] Stretching strains with ε values of 90% and 120% are defined as "non-injury" and "injury" stimuli for the emulation. Figures 5(e) and 5(f) show the typical EPSC responses triggered by a single "non-injury" stretching strain after experiencing the "non-injury" and "injury" strains, respectively. Here, a current threshold of 50 μA is set for the analogue of a pain threshold. Under the first "non-injury" and "injury" strains, the peak EPSC values are ∼ 43.8 μA and ∼ 78.3 μA, respectively. At the second "non-injury" strain, the peak EPSC values are ∼ 45.7 μA and ∼ 56.4 μA after experiencing the "non-injury" and "injury" strains, respectively. The increased response to the same "non-injury" stimulus after a prior "injury" stimulus demonstrates a thresholdbased sensitization effect, which is conceptually analogous to hyperalgesia in biological systems. It should be noted here that this is a simplified electrical emulation and does not capture the full complexity of biological pain pathways. A learninglike behavior can also be mimicked by the present sensory neuron, as shown in Fig. 5(g). The peak EPSC value of 156 μA is set as a learning threshold. During the first training stage, continuous stretching with ε of 120% and frequency of 2 Hz for 8 times results in an EPSC value of 157 μA. After releasing for 30 s, the EPSC drops to ∼ 19 μA. At the second training stage, continuous stretching for 8 times results in an EPSC value of ∼ 166 μA, much higher than the threshold. However, continuous stretching for 4 times is enough to reach the threshold. After releasing for 30 s, the EPSC value drops to ∼ 24 μA. At the third training stage, continuous stretching for 8 times results in the EPSC value of ∼ 168 μA, mimicking a progressively enhanced response with repeated training. After releasing for 30 s, the EPSC value drops to ∼ 21.6 μA. These results show an analogue electronic emulation of "learning-forgetting-relearning" dynamics based on cumulative proton effects. However, it should be noted here that the present activities have not replicated the molecular or circuit mechanisms of biological learning.

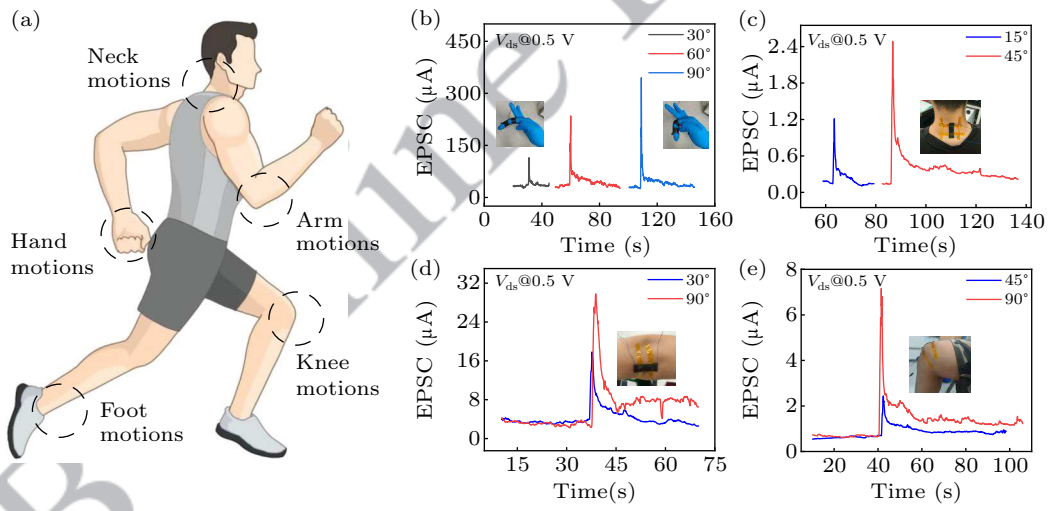


Fig. 6. (a) Schematic diagram of human body movement states. (b) EPSC responses at different flexion angles of the finger joints. (c) EPSC responses at different flexion angles of the neck joints. (d) EPSC responses at different elbow flexion angles. (e) EPSC responses at different knee flexion angles.

These results indicate that the present bionic motion sensory neuron can efficiently perceive and record mechanical activities such as body joint bending and mechanical motion, as schematically shown in Fig. 6(a). Since the strain range of human motion is below 75%, the present sensory neuron has great potential for monitoring human movements. Figure 6(b) demonstrates the ability to track bending movements of human finger joints. As the bending angle of the finger joints increases from 30° to 90°, the η value increases. Thus, the V_{SRS} value increases accordingly, inducing an increase in the peak EPSC value from ∼ 115 nA to ∼ 345 nA. Figure 6(c) illustrates the EPSC response used to monitor neck bending when a volunteer looks down. The peak EPSC values are ∼ 1.2 μA and ∼ 2.5 μA for angles of 15° and 45°, respectively. Similarly, the present sensory neuron can also accurately monitor strain signals generated during elbow and knee bending, as shown in Figs. 6(d) and 6(e), respectively. This highlights the potential of the present bionic sensory neuron in fields such as human health monitoring, neural prosthetics, and human-machine interfacing.

3. Conclusion

In summary, a stretchable bionic motion sensory neuron is proposed by integrating an ITO neuromorphic transistor and a stretchable resistive sensor. The sensor is fabricated using Ecoflex silicone as the substrate, doped with carbon black and multi-walled carbon nanotubes. It demonstrates high sensi-

CPB In Press

tivity with a gauge factor of up to 32, offering a wide detection range with mechanical tensile strain of up to 200%. The sensory neuron can operate at low voltages due to the low operating voltage of the chitosan-gated ITO neuromorphic transistor. Thus, the bionic motion sensory neuron can accurately sense external strain and exhibit typical synaptic responses with strain applied to the SRS. Since strain applied to the sensors can carry information, the sensory neuron shows signal encoding and decoding capabilities based on the Morse code alphabet. In addition, it allows real-time monitoring of joint bending activities. Thus, the sensory neuron holds potential for wearable electronics and provides interesting ideas for neural prosthetics and smart human-machine interface technologies.

Acknowledgments

Project supported by the National Natural Science Foundation of China (Grant No. U22A2075) and the Ningbo Key Scientific and Technological Project (Grant No. 2021Z116).

References

[1] Jung U, Kim M, Jang J, Bae J H, Kang I M and Lee S H 2024 *Adv. Sci.* **11** 2307494
[2] Huang H X, Shi S H, Zha J J, Xia Y P, Wang H D, Yang P, Zheng L, Xu S C, Wang W, Ren Y, Wang Y J, Chen Y, Chan H P, Ho J C, Chai Y, Wang Z R and Tan C L 2025 *Nat. Commun.* **16** 3836
[3] Seo S, Kim B, Kim D, Park S, Kim T R, Park J, Jeong H, Park S O, Park T, Shin H, Kim M S, Choi Y K and Choi S 2022 *Nat. Commun.* **13** 6431
[4] Yang H L, Lam K Y, Xiao L, Xiong Z H, Hu H, Niyato D and Poor H V 2022 *Nat. Commun.* **13** 4269
[5] Rafique H, Abbas G, Mendes M J, Barquinha P, Martins R, Fortunato E, Águas H and Jana S 2026 *Nano-Micro Lett.* **18** 44
[6] Mead C 1990 *Proc. IEEE* **78** 1629
[7] Roy K, Jaiswal A and Panda P 2019 *Nature* **575** 607
[8] Gao B, Zhou Y, Zhang Q T, Zhang S L, Yao P, Xi Y, Liu Q, Zhao M R, Zhang W Q, Liu Z W, Li X Y, Tang J S, Qian H and Wu H Q 2022 *Nat. Commun.* **13** 2026
[9] Prezioso M, Merrikh-Bayat F, Hoskins B D, Adam G C, Likharev K K and Strukov D B 2015 *Nature* **521** 61
[10] Kim D E, Chabungbam A S, Kim G, Son J, Lim B M, Lee Y M, Kim S J, Kim M, Lee H S and Park H H 2025 *Adv. Funct. Mater.* **35** 2503883
[11] Zhu L Q, Wan C J, Guo L Q, Shi Y and Wan Q 2014 *Nat. Commun.* **5** 3158
[12] Guo F, Song M L, Wong M C, Ding R, Lo W F, Pang S Y, Jie W J and Hao J H 2022 *Adv. Funct. Mater.* **32** 2108014
[13] Kim Y, Chortos A, Wu W T, Liu Y X, Oh J Y, Son D, Kang J, Foudeh A M, Zhu C X, Lee Y, Niu S M, Liu J, Pfattner R, Bao Z N and Lee T W 2018 *Science* **360** 998
[14] Sahoo S, Varghese A, Sadashiva A, Goyal M, Sakhuja J, Bhowmik D and Lodha S 2025 *ACS Nano* **19** 13287
[15] Sun Y L, Qian L, Xie D, Lin Y X, Sun M X, Li W W, Ding L M, Ren T L and Palacios T 2019 *Adv. Funct. Mater.* **29** 1902538
[16] Shastri B J, Tait A N, de Lima T F, Pernice W H P, Bhaskaran H, Wright C D and Prucnal P R 2021 *Nat. Photonics* **15** 102
[17] Yue K, Liu Y Z, Lake R K and Parker A C 2019 *Sci. Adv.* **5** eaau8170
[18] Ranjan A, Farooq T, Chi C C, Sung H Y, Padilla R I S, Lin P H, Wu W W, Lu M Y, Mishra R and Lai C H 2025 *Nano Lett.* **25** 7089
[19] Chen S S, Liu Y, Wang Z A, Colonell J, Liu L D, Hou H, Tien N W, Wang T, Harris T, Druckmann S, Li N and Svoboda K 2024 *Cell* **187** 676
[20] Rungreungthanapol T, Homma C, Akagi K, Tanaka M, Kikuchi J, Tomizawa H, Sugizaki Y, Isobayashi A, Hayamizu Y and Okochi M 2023 *Anal. Chem.* **95** 4556
[21] Yang L, Wang Z X, Zhang S, Li Y, Jiang C P, Sun L and Xu W T 2022 *Nano Lett.* **23** 8
[22] Lu Y T, Rao Z L Y, Shim H, Song Y M, Fan Z Y, Guo C F and Yu J 2026 *Nat. Electron.* **9** 180
[23] Wang W S, Zhou S Y, Gong B C, Di J K, Zhang W L, Li B B, Wu L F, Xiao H and Zhu L Q 2025 *Adv. Funct. Mater.* e19137
[24] Zhang K T, Huo Z W, Wang Y F, Yan H, Yu J R, Cheng L Q, Fu Y X, Liu C, Li Z H, Liu Z, Wang Z L, Sun Q J and Lin X D 2025 *Nano Energy* **144** 111399
[25] Zhou S Y, Li B B, Wang W S, Gong B C, Di J K and Zhu L Q 2026 *Front. Phys.* **21** 024203
[26] Wen S K, Liu Y N, Li Y, Xie L, Li J and Zhang J H 2024 *Int. J. Extrem. Manuf.* **7** 025506
[27] Huang X, Zhou S Y, Wang W S, Huang Y J, Gong B C, Di J K, Hui X and Zhu L Q 2025 *J. Mater. Chem. C* **13** 9593
[28] Hao Y N, Yan Q Y, Liu H J, He X Y, Zhang P H, Qin X H, Wang R R, Sun J, Wang L M and Cheng Y 2023 *Adv. Funct. Mater.* **33** 2303881
[29] Wu X P, Luo X M, Song Z M, Bai Y Y, Zhang B and Zhang G P 2023 *Adv. Funct. Mater.* **33** 2303504
[30] Yang Y, Cui T R, Li D, Ji S R, Chen Z K, Shao W C, Liu H F and Ren T L 2022 *Nano-Micro Lett.* **14** 161
[31] Kang D, Pikhitsa P V, Choi Y W, Lee C, Shin S S, Piao L F, Park B, Suh K Y, Kim T and Choi M 2014 *Nature* **516** 222
[32] Li J C, Liu J, Peng C R, Liu X M, Wu Z W and Zheng F J 2022 *Micromachines* **13** 619
[33] Zhou Z Y, Tang W R, Xu T, Zhao W Y, Zhang J J and Bai C W 2024 *Sensors* **24** 4793
[34] Mostafalu P, Tamayol A, Rahimi R, Ochoa M, Khalilpour A, Kiaee G, Yazdi I K, Bagherifard S, Dokmeci M R, Ziaie B, Sonkusale S R and Khademhosseini A 2018 *Small* **14** 1703509
[35] Moniruzzaman M, Yin Z Z, Hossain M S B, Choi H and Guo Z S 2023 *IEEE J. Biomed. Health Inform.* **27** 5345
[36] Wang T H, Jin T, Lin W Y, Lin Y Q, Liu H F, Yue T, Tian Y Z, Li L, Zhang Q and Lee C K 2024 *ACS Nano* **18** 9980
[37] Wang Y R, Liu D X, Zhang Y M, Fan L C, Ren Q Q, Ma S H and Zhang M 2022 *ACS Nano* **16** 8283
[38] Wang K X, Yap L W, Gong S, Wang R, Wang S J and Cheng W L 2021 *Adv. Funct. Mater.* **31** 2008347
[39] Ma L J, Lei X, Guo X Q, Wang L H, Li S F, Shu T, Cheng G J and Liu F 2022 *ACS Appl. Nano Mater.* **5** 7142
[40] Chen M, Luo W F, Xu Z Q, Zhang X P, Xie B, Wang G H and Han M 2019 *Nat. Commun.* **10** 4024
[41] Huang J, Zhou J, Luo Y M, Yan G, Liu Y, Shen Y P, Xu Y, Li H L, Yan L B, Zhang G H, Fu Y Q and Duan H G 2020 *ACS Appl. Mater. Interfaces* **12** 43009
[42] Amjadi M, Pichitpajongkit A, Lee S, Ryu S and Park I 2014 *ACS Nano* **8** 5154
[43] Xu S, Rezvanian O, Peters K and Zikry M A 2013 *Nanotechnology* **24** 155706
[44] Xia J F, He L, Lu Z L, Song J N, Wang Q S, Liu L P and Tian Y L 2023 *ACS Appl. Nano Mater.* **6** 19279
[45] Sun L J, Huang H F, Zhang L Z, Neisiany R E, Ma X P, Tan H and You Z W 2024 *Adv. Sci.* **11** 2305697
[46] Tashakori A, Jiang Z A, Servati A, Soltanian S, Narayana H, Le K, Nakayama C, Yang C L, Wang Z J and Eng J J 2024 *Nat. Mach. Intell.* **6** 106
[47] Stetter B J, Ringhof S, Krafft F C, Sell S and Stein T 2019 *Sensors* **19** 3690
[48] He Y L, Nie S, Liu R, Jiang S S, Shi Y and Wan Q 2019 *Adv. Mater.* **31** 1900903
[49] Huang Y J, Wu L F, Di J K, Huang X, Wang W S, Zhou S Y, Gong B C and Zhu L Q 2025 *Front. Phys.* **20** 034205
[50] Zucker R S and Regehr W G 2002 *Annu. Rev. Physiol.* **64** 355
[51] Zhou S Y, Huang X, Wang W S, Gong B C, Di J K, Huang Y J and Zhu L Q 2025 *IEEE Trans. Electron Devices* **72** 845
[52] Jiang H F, Ji H F, Ma Z Z, Yang D W, Ma J L, Zhang M Y, Li X, Wang M, Li Y, Chen X, Wu D, Li X J, Shan C X and Shi Z F 2024 *Light Sci. Appl.* **13** 316
[53] Arber S 2017 *EMBO Mol. Med.* **9** 281
[54] Dubin A E and Patapoutian A 2010 *J. Clin. Invest.* **120** 3760
[55] Basbaum A I, Bautista D M, Scherrer G and Julius D 2009 *Cell* **139** 267

Chinese Physics